Available online at www.sciencedirect.com
SCIENCE DIRECT®
Journal of Solid State Chemistry 179 (2006) 605–612
JOURNAL OF SOLID STATE CHEMISTRY
www.elsevier.com/locate/jssc

Structural phase transition and magnetic properties of double perovskites Ba_2CaMO_6 (M = W, Re, Os)

Kazuhiro Yamamura*, Makoto Wakeshima, Yukio Hinatsu

Division of Chemistry, Graduate School of Science, Hokkaido University, Sapporo 060-0810, Japan

Received 19 July 2005; received in revised form 3 October 2005; accepted 5 October 2005
Available online 4 January 2006

Abstract

Structures and magnetic properties for double perovskites Ba_2CaMO_6 (M = W, Re, Os) were investigated. Both Ba_2CaReO_6 and Ba_2CaWO_6 show structural phase transitions at low temperatures. For Ba_2CaReO_6, the second order transition from cubic $Fm\bar{3}m$ to tetragonal $I4/m$ has been observed near 120 K. For Ba_2CaWO_6, the space group of the crystal structure is $I4/m$ at 295 K and the transition to monoclinic $I2/m$ has been observed between 220 K. Magnetic susceptibility measurements show that Ba_2CaReO_6 ($S = 1/2$) and Ba_2CaOsO_6 ($S = 1$) transform to an antiferromagnetic state below 15.4 and 51 K, respectively. Anomalies corresponding to their structural phase transition and magnetic transition have been also observed through specific heat measurements.

Keyword: Perovskite; Magnetic properties; Rhenium; Osmium; Oxide; Magnetic susceptibility; Specific heat; Antiferromagnetic transition; Structural phase transition

1. Introduction

Recently, mixed metal oxides containing 5*d* transition metals have attracted a great deal of interest. For instance, a pyrochlore-type oxide $Cd_2Re_2O_7$ and defected pyrochlore-type oxides $AOsO_6$ (A = K, Rb, Cs) show superconductivity [1–4]. Peculiar electric and magnetic properties have been observed for double perovskite-type oxides A_2FeReO_6 (A = Ba, Sr, Ca). All these A_2FeReO_6 are ferrimagnetic with high transition temperatures [5,6]. Furthermore, for A = Ba and Sr, they are metallic conductors and show negative magnetoresistance effect [7–9]. On the other hand, it has been reported that Ca_2FeReO_6 show a metal–insulator transition [10]. These studies have been progressed from the viewpoint of frustration systems or the correlation between 5*d* and 3*d* transition metals. However, little is known on the behavior of 5*d* electrons in solids.

Stitzer et al. reported the magnetic properties of two double perovskites: Ba_2LiOsO_6 and Ba_2NaOsO_6 [11]. In these compounds, the osmium ions are in the septavalent state. Since the electronic configuration of the Os^{7+} ions is [Xe] $4f^{14}$ $5d^1$ ([Xe]: Xe electronic core), magnetic properties of these compounds are due to the behavior of its 5*d* electron. The effective magnetic moments of Ba_2LiOsO_6 and Ba_2NaOsO_6 are 0.733 and 0.677 μ_B, respectively [11]. These values are much smaller than the theoretical moment 1.73 μ_B, which is unclear at present.

We focus our attention on double perovskite-type oxides containing 5*d* elements Ba_2CaMO_6 (M = W, Re, Os) in which Ca and M are ordered. The structures of Ba_2CaMO_6 are reported to be cubic double perovskite [12,13], which indicates that M ions are in an ideal octahedral crystal field formed by six oxide ions. In these compounds, M ions are considered to be in the hexavalent state and the unpaired electrons for W^{6+}, Re^{6+}, and Os^{6+} are $5d^0$, $5d^1$, and $5d^2$, respectively. Therefore, we expect to obtain the information on the behavior of 5*d* electrons in solids by studying magnetic properties of this series of compounds.

In this paper, we will report crystal structures and magnetic properties of Ba_2CaMO_6 through their X-ray diffraction (XRD), magnetic susceptibility and specific heat measurements at low temperatures.

*Corresponding author. Fax: +81 11 746 2557.
E-mail address: wake@sci.hokudai.ac.jp (K. Yamamura).

0022-4596/$ - see front matter © 2005 Published by Elsevier Inc.
doi:10.1016/j.jssc.2005.10.003

2. Experimental

Ba_2CaMO_6 (M = W, Re, Os) were prepared with the solid-state reaction.

(1) Ba_2CaWO_6: Starting materials were barium carbonate ($BaCO_3$), calcium carbonate ($CaCO_3$) and tungsten trioxide (WO_3). These reagents were weighed in appropriate metal ratios and ground in an agate mortar. The mixtures were pressed into pellets and were calcined at 1173 K. The calcined materials were reground and sintered at 1573 K for 48 h with intermediate regrindings and repelletizings.

(2) Ba_2CaReO_6: As starting materials, barium peroxide (BaO_2), calcium monoxide (CaO), rhenium metal (Re), and rhenium dioxide (ReO_2) were used. The stoichiometric mixtures were ground, pressed into pellets, and sealed in an evacuated silica ampoule. The ampoule was heated at 1173 K for 6 h with intervening regrinding and repelletizing steps.

(3) Ba_2CaOsO_6: BaO_2, CaO and osmium metal (Os) were mixed stoichiometrically. Due to evaporation of OsO_4, additional amounts of Os (10 mol%) were added. The pelletized mixtures were heated in air at 1273 K for 15 min. Rapid heating and quenching were needed to prepare Ba_2CaOsO_6.

Powder XRD measurements were carried out in the region of $10^\circ \leqslant 2\theta \leqslant 120^\circ$ in the temperature range 17–295 K with a Rigaku RINT 2100 diffractmeter using Cu$K\alpha$ radiation equipped with a curved graphite monochromator. Collected diffraction data were analyzed by the Rietveld technique using the program RIETAN 2000 [14].

Temperature dependence of magnetic susceptibilities was measured under both zero-field cooled (ZFC) condition and field cooled (FC) condition in the temperature range of 1.8–400 K in a magnetic field of 0.1 T with a SQUID magnetometer (Quantum Design, model MPMS-5S). Magnetization measurements were performed at a temperature of 5 K in the magnetic field range of $-5\,\mathrm{T} \leqslant \mu_0 H \leqslant 5\,\mathrm{T}$.

Heat capacity measurements were carried out using a relaxation technique supplied by the commercial heat capacity measurement system (Quantum Design, PPMS) in the temperature range of 2–300 K. The samples in the form of a pellet (~15 mg) were mounted on an alumina plate with Apiezon N-grease for better thermal contact.

3. Results and discussion

3.1. Crystal structures

Ba_2CaMO_6 (M = W, Re, Os) is reported to be crystallized in the cubic double perovskite-type structure (S.G. $Fm\bar{3}m$) at room temperature [12,13]. For Ba_2CaReO_6 and Ba_2CaOsO_6, their lattice parameters determined at 295 K are consistent with the reported parameters [13].

Fig. 1 shows the XRD pattern of Ba_2CaOsO_6 at 17 K. The structure was refined by applying the space group $Fm\bar{3}m$, which means that Ba_2CaOsO_6 keeps cubic double perovskite-type structure down to 17 K.

Fig. 2 shows the change in the XRD pattern against temperature for Ba_2CaReO_6 in the range of $75^\circ \leqslant 2\theta \leqslant 100^\circ$. In the temperature range between 130 and 295 K, all the XRD data were fitted with the structure model with the space group $Fm\bar{3}m$. When the temperature was decreased through 120 K, some diffraction peaks was split. This peak splitting is obvious at 17 K. For example, the diffraction peak at $2\theta \sim 95^\circ$ which is indexed to be (008) for cubic perovskite splits into (008) and (440). This structural phase transition from the cubic symmetry to the tetragonal one has been often observed for other double perovskites such as Sr_2CaWO_6 and Sr_2MgWO_6 [15]. According to Howard et al., the subgroups of the $Fm\bar{3}m$ with the tetragonal double perovskite-type structure are $P4/mnc$ and $I4/m$ [16]. We attempted to analyze the present diffraction data obtained at low temperatures with the corresponding two

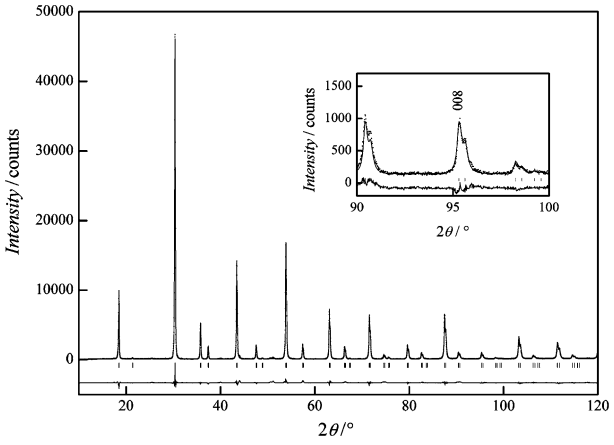

Fig. 1. Powder XRD pattern for Ba_2CaOsO_6 at 17 K. The inset show the XRD pattern in the region of $90^\circ \leqslant 2\theta \leqslant 100^\circ$ at 17 K.

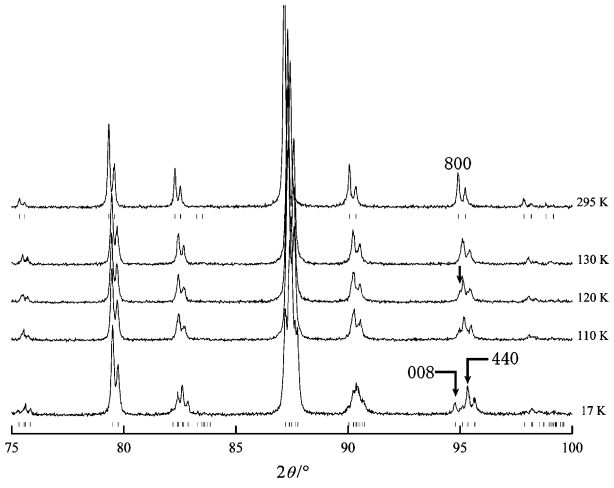

Fig. 2. Temperature dependence of the XRD pattern for Ba_2CaReO_6 in the region of $75^\circ \leqslant 2\theta \leqslant 100^\circ$ in the temperature range 17–295 K.

different structural models. Refinement of the structure by the model with space group $P4/mnc$ gave a result worse ($R_{wp} = 15.99$, $R_I = 3.13$, $S = 1.66$) than that with the $I4/m$ model ($R_{wp} = 15.94$, $R_I = 3.00$, $S = 1.65$) at 17 K; therefore, we think that the model with the space group $I4/m$ is a more valid one below 120 K.

In the case of Ba_2CaWO_6, a more complicated change of XRD pattern against temperature was observed. Fig. 3 shows the change of XRD patterns for Ba_2CaWO_6 in the range of $75^\circ \leqslant 2\theta \leqslant 100^\circ$. The diffraction peaks at 295 and 250 K were indexed based on the tetragonal symmetry. After refinement, it turned out that the $I4/m$ model gave good calculation results at both 295 and 250 K. When the temperature is decreased through 200 K, some diffraction peaks were split. A peak indexed to be (404) for tetragonal perovskites split into three peaks, which are indexed to be (404), (044) and (−404) for monoclinic ones. Therefore, we attempted to analyze all the diffraction data with three monoclinic structural models, i.e. $C2/c$, $P2_1/n$ and $I2/m$. At 200 K, the refinement with the $C2/c$ model gave results worse ($R_{wp} = 13.21$, $R_I = 2.76$, $S = 1.45$) than those with the other structure models. There is little difference between the results of $P2_1/n$ model ($R_{wp} = 11.74$, $R_I = 1.90$, $S = 1.29$) and that of $I2/m$ model ($R_{wp} = 12.05$, $R_I = 1.86$, $S = 1.32$). However, the standard deviations of the fractional coordinates of oxygen atoms are too big for the $P2_1/n$ model (for example, O1 site (0.283(14), 0.242(12), 0.007(10)) for $P2_1/n$ model against (0.252(6), 0.734(6), 0.025(3)) for $I2/m$ model). Similar results were obtained at 17 K. Therefore, we concluded that Ba_2CaWO_6 has the structure with $I2/m$ at low temperature. Since $I2/m$ is the subgroup of $I4/m$ [17], the transition observed for Ba_2CaWO_6 with decreasing temperature through 200–250 K is the second order structural phase transition $I4/m \rightarrow I2/m$. It is known that Sr_2BWO_6 (B = Ca, Mg) [15] and Ba_2CaReO_6 show the structural phase transition $I4/m \rightarrow Fm\bar{3}m$ with increasing temperature. In view of this fact, Ba_2CaWO_6 is expected to have the similar

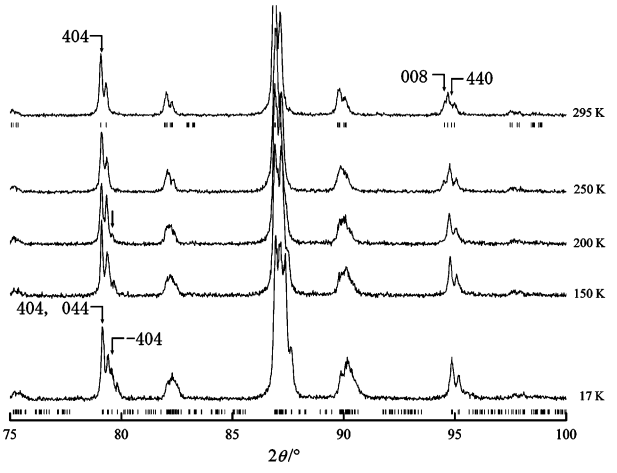

Fig. 3. Temperature dependence of the XRD pattern for Ba_2CaWO_6 in the region of $75^\circ \leqslant 2\theta \leqslant 100^\circ$ in the temperature range 17–295 K.

transition at higher temperatures. Table 1 shows the lattice constants, the structural parameters and the R factors for Ba_2CaMO_6 at 295 and 17 K.

Fig. 4 shows the crystal structure of Ba_2CaMO_6. As is well known, the MO_6 and CaO_6 octahedrons are alternately arranged with corner sharing and Ba ions are coordinated by 12 oxide ions. Glazer proposed a simple method for clarifying the space group of perovskite by octahedral tilting [18], and Woodward applied it to the double perovskite $A_2BB'O_6$ [19]. According to Glazer's notation, double perovskite-type structures with the space group $Fm\bar{3}m$, $I4/m$, and $I2/m$ are described as $a^0a^0a^0$, $a^0a^0c^-$, and $a^0b^-b^-$, respectively. The differences in structures for the double perovskites are attributed to the different tilting system.

When the unit cell of primitive perovskites ABO_3 is described as $a_p \times b_p \times c_p$ ($a_p = b_p = c_p$ for cubic, $a_p = b_p$ for tetragonal), that of double-type perovskites should be described as $2a_p \times 2a_p \times 2a_p$ (cubic) or $\sqrt{2}a_p \times \sqrt{2}b_p \times 2c_p$ (tetragonal or monoclinic). Fig. 5 shows the temperature dependence of the lattice parameters a_p, b_p, c_p, β and the cell volume V_p (where the subscript p indicates the unit cell of the primitive perovskites ABO_3) of Ba_2CaMO_6. With decreasing temperature, the lattice parameter β for Ba_2CaWO_6 decreases from 90° (see Fig. 5(a)), which indicates that the crystal structure becomes more distorted.

The temperature dependence of the lattice parameters a_p, c_p, and V_p for Ba_2CaReO_6 are shown in Figs. 5(b) and (c), respectively. Although a_p and V_p decrease with decreasing temperature, c_p increases, which indicates that the structure is more distorted with decreasing temperature.

For all Ba_2CaMO_6 compounds, V_p (Fig. 5(c)) decrease monotonically with decreasing temperature, which indicates the shrinking of the unit cell.

Of Ba_2CaMO_6, Ba_2CaWO_6 has the largest V_p, and Ba_2CaOsO_6 has the smallest (see Fig. 5(c)). This result directly reflects the ionic radii of M ions. The ionic radii of M^{6+} ions in six-coordinates are $r_W = 0.60$ Å, $r_{Re} = 0.55$ Å, and $r_{Os} = 0.545$ Å [20]. The difference in the ionic radii also affects the crystal structure of Ba_2CaMO_6. The stability of perovskites ABO_3 is generally estimated by the tolerance factor t. This factor is defined by

$$t = \frac{r_A + r_O}{\sqrt{2}(r_B + r_O)}, \quad (1)$$

where r_A, r_B, and r_O are the ionic radii of the respective ions. In double perovskites $A_2B'B''O_6$, r_B is the average value between $r_{B'}$ and $r_{B''}$. For an ideal cubic perovskite structure, the value of t is equal or near to unity, whereas for the structure distorted from cubic symmetry, the value of t is <1. The tolerance factors for Ba_2CaMO_6 compounds with M = W, Re and Os are obtained to be 0.967, 0.979, and 0.980, respectively at room temperature. These values allow us to expect that the structures of Ba_2CaMO_6 (M = Re and Os) should be pseudo-cubic

Table 1
Lattice parameters, structural parameters and R factors of Ba_2CaMO_6 (M = W, Re, Os) at 295 K and 17 K. All isotropic displacement parameters were fixed

Atom	Site	x	y	z	B (Å^2)
(a) Ba_2CaWO_6					
(1) 295 K (S.G. $I4/m$)					
Ba	4*d*	0	1/2	1/4	0.4
Ca	2*b*	0	0	1/2	0.6
W	2*a*	0	0	0	0.3
O1	4*e*	0	0	0.223 (3)	1.0
O2	8*h*	0.211 (3)	0.275 (2)	0	1.0
$a = 5.930(1)$ Å, $c = 8.397(1)$ Å, $R_{wp} = 11.58$, $R_p = 8.01$, $R_I = 2.55$, $S = 1.37$					
(2) 17 K (S.G. $I2/m$)					
Ba	4*i*	0.4974 (1)	1/2	0.248 (1)	0.4
Ca	2*c*	1/2	0	0	0.6
W	2*b*	0	1/2	0	0.3
O1	4*i*	0.530 (9)	0	0.275 (5)	1.0
O2	8*j*	0.253 (5)	0.724 (5)	0.020 (2)	1.0
$a = 5.910(5)$ Å, $b = 5.929(5)$ Å, $c = 8.375(7)$ Å, $\beta = 89.74(1)^\circ$, $R_{wp} = 11.11$, $R_p = 7.40$, $R_I = 1.81$, $S = 1.43$					
(b) Ba_2CaReO_6					
(1) 295 K (S.G. $Fm\bar{3}m$)					
Ba	8*c*	1/4	1/4	1/4	0.4
Ca	4*b*	1/2	1/2	1/2	0.6
Re	4*a*	0	0	0	0.3
O	24*e*	0.233 (1)	0	0	1.0
$a = 8.371(4)$ Å, $R_{wp} = 15.89$, $R_p = 10.01$, $R_I = 2.98$, $S = 1.59$					
(2) 17 K (S.G. $I4/m$)					
Ba	4*d*	0	1/2	1/4	0.4
Ca	2*b*	0	0	1/2	0.6
Re	2*a*	0	0	0	0.3
O1	4*e*	0	0	0.231 (2)	1.0
O2	8*h*	0.212 (2)	0.257 (3)	0	1.0
$a = 5.896(1)$ Å, $c = 8.375(1)$ Å, $R_{wp} = 15.94$, $R_p = 10.24$, $R_I = 2.99$, $S = 1.65$					
(c) Ba_2CaOsO_6					
(1) 295 K (S.G. $Fm\bar{3}m$)					
Ba	8*c*	1/4	1/4	1/4	0.4
Ca	4*b*	1/2	1/2	1/2	0.6
Os	4*a*	0	0	0	0.3
O	24*e*	0.233 (1)	0	0	1.0
$a = 8.359(5)$ Å, $R_{wp} = 7.52$, $R_p = 5.24$, $R_I = 2.62$, $S = 1.64$					
(2) 17 K (S.G. $Fm\bar{3}m$)					
Ba	8*c*	1/4	1/4	1/4	0.4
Ca	4*b*	1/2	1/2	1/2	0.6
Os	4*a*	0	0	0	0.3
O	24*e*	0.241 (1)	0	0	1.0
$a = 8.344(5)$ Å, $R_{wp} = 8.52$, $R_p = 5.53$, $R_I = 2.22$, $S = 1.86$					

Note. $R_{wp} = \left[\sum w_i(y_i - f_i(x))^2 / \sum w_i y_i\right]^{1/2}$, $R_p = \sum |y_i - f_i(x)| / \sum y_i$ and $R_I = \sum |I_k(\text{obs}) - I_k(\text{cal})| / \sum I_k(\text{obs})$.

perovskite-type. The tolerance factor for Ba_2CaWO_6 is smaller than those for other compounds, and this compound is tetragonal at room temperature.

3.2. Magnetic properties

Fig. 6 shows the temperature dependences of the reciprocal magnetic susceptibilities for Ba_2CaMO_6 (M = Re and Os). An anomaly in the susceptibility vs. temperature curve has been found for M = Re and Os at 15.4 and 51 K, respectively.

Magnetization measurements were carried out at 5 K to investigate the origin for these anomalies. Fig. 7 shows magnetization curves for Ba_2CaReO_6 and Ba_2CaOsO_6. For Ba_2CaReO_6, there exists no hysteresis loop, and magnetization is not saturated even at 5 T; therefore, the anomaly observed in magnetic susceptibility vs. temperature curve is due to a normal antiferromagnetic transition.

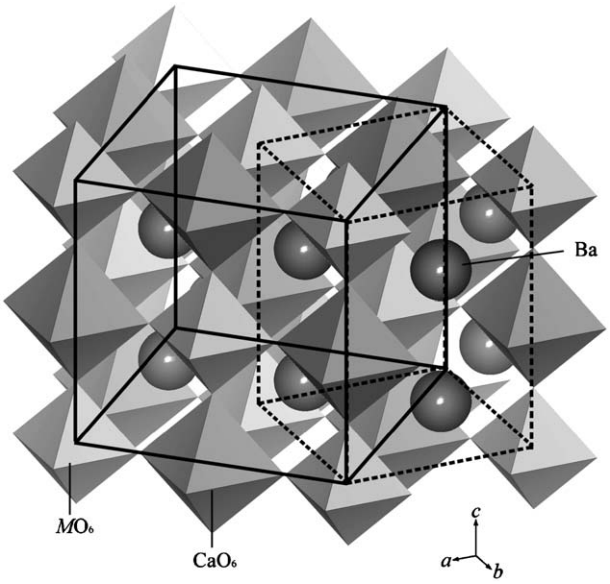

Fig. 4. Crystal structures of Ba_2CaMO_6. Solid and dotted lines show the cubic cell and the tetragonal cell, respectively.

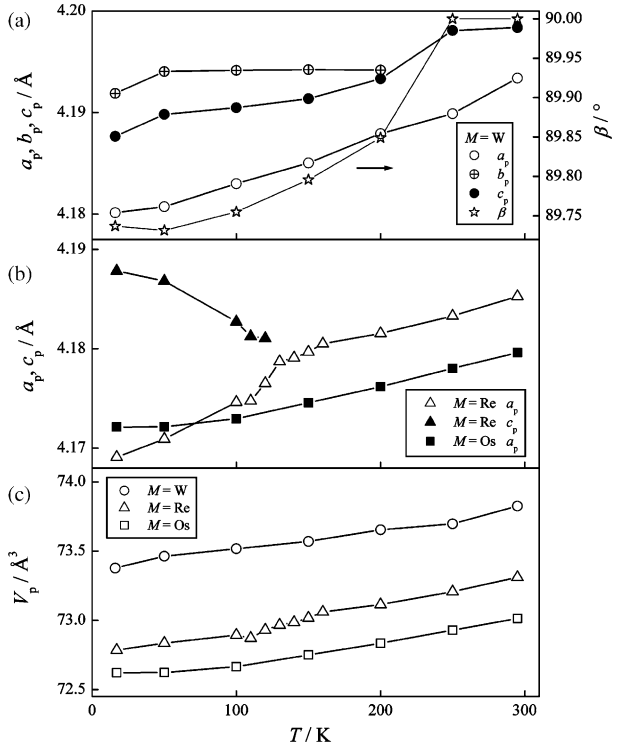

Fig. 5. Temperature dependences of lattice parameters and cell volumes of primitive perovskite-type structures for Ba_2CaMO_6 (see the text).

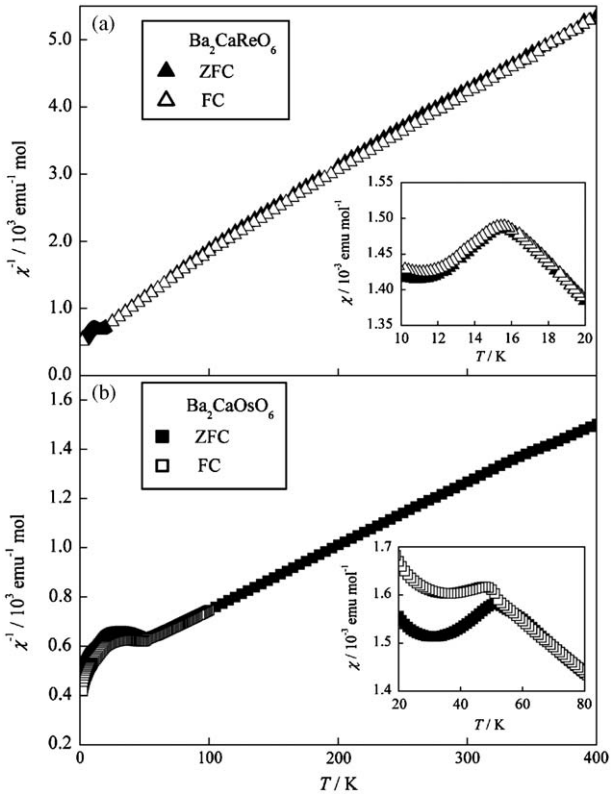

Fig. 6. Temperature dependences of the reciprocal magnetic susceptibilities for (a) Ba_2CaReO_6 and (b) Ba_2CaOsO_6. The insets display the detailed susceptibilities in the vicinity of magnetic transition temperatures.

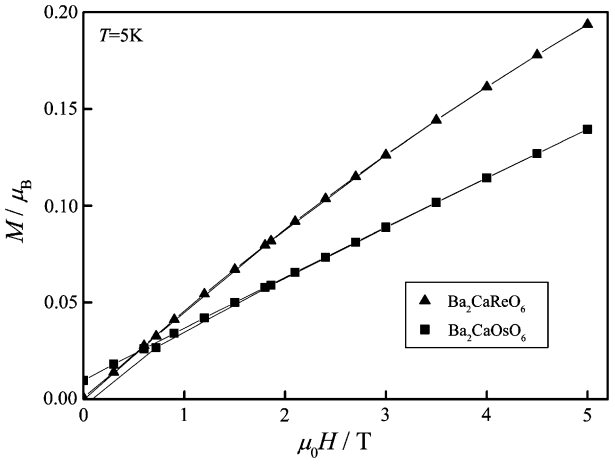

Fig. 7. Magnetic field dependence of the magnetization for Ba_2CaMO_6 (M = Re and Os) measured at 5 K.

Although the Os^{6+} ion has more spins ($S = 1$) than the Re^{6+} ion ($S = 1/2$), the magnetization for Ba_2CaOsO_6 is smaller than that for Ba_2CaReO_6. This suppression of the magnetization implies that there exists the stronger antiferromagnetic interaction in Ba_2CaOsO_6. In addition, as will be described later, specific heat measurements show an anomaly at the temperature at which the maximum is observed in the magnetic susceptibility vs. temperature curve, which indicates that this anomaly is due to the long range magnetic ordering. For these reasons, we conclude that the magnetic transition observed for Ba_2CaOsO_6 at 51 K is the antiferromagnetic transition. The divergence between ZFC and FC magnetic susceptibilities and the existence of small magnetic hysteresis loop at 5 K indicate that there is a very weak ferromagnetic component in this antiferromagnetic interaction.

In the temperature range 100–400 K, their magnetic susceptibilities are fitted using the Curie–Weiss law

$$\chi = \frac{C}{T-\theta} + \chi_{TIP}, \quad (2)$$

where χ_{TIP} is the temperature-independent term. The effective magnetic moments μ_{eff} and Weiss constants θ are obtained, and they are listed in Table 2.

For Re^{6+} ($5d^1$) and Os^{6+} ($5d^2$), the calculated spin-only effective magnetic moments are 1.73 and 2.83 μ_B, respectively. The obtained effective magnetic moments, 0.744 μ_B for Ba_2CaReO_6 and 1.61 μ_B for Ba_2CaOsO_6, are smaller than the calculated ones. Let us compare the effective magnetic moments for these two compounds with those for similar compounds. Recently, it was reported that the effective magnetic moments for Ba_2LiOsO_6, Ba_2NaOsO_6, Sr_2MgReO_6, and Sr_2CaReO_6 are 0.733, 0.677, 1.72, and 1.659 μ_B, respectively, in which the Os (Re) ions have the unpaired $5d^1$ electron [11,21,22]. It is obvious that there is a large difference in the effective magnetic moments between Ba compounds and Sr compounds. The reason for this lies in the strength of the spin–orbit coupling. The Ba compounds are cubic [11]. On the other hand, Sr_2MgReO_6 and Sr_2CaReO_6 are tetragonal and monoclinic, respectively [21,22]. The degeneracy of $5d$ orbital is lifted in the distorted structure, which quenches the orbital angular momentum. As a result, we need not consider the effect of the spin–orbit coupling, and the effective magnetic moment is calculated only by the spin angular momentum. In contrast, in the regular octahedral crystal field, the spin–orbit coupling is effective and reduces the effective magnetic moment.

The large negative Weiss constants (see Table 3) are indicative of the presence of predominant antiferromagnetic interaction. According to the molecular field theory [23], the nearest neighbor (NN) exchange constants J_1 can be calculated by

$$J_1/k_B = \frac{\theta}{z_1(2/3)S(S+1)}, \quad (3)$$

where k_B, z_1 and S are Boltzmann constants, the number of NN magnetic ions and spin quantum number, respectively. Table 3 also lists the J_1/k_B for Ba_2CaReO_6, Ba_2CaOsO_6 and some analogous compounds. The value for Ba_2CaReO_6 is smaller than that for Ba_2CaOsO_6. It corresponds to the result that Ba_2CaOsO_6 has a higher magnetic transition temperature. In general, the values for J_1/k_B are comparable for Ba compounds, which indicates that the electronic states of Re (Os) ions in these compounds are quite similar. On the other hand, Sr compounds have much larger J_1/k_B values than those for Ba compounds despite the distorted exchange pathway. Wiebe et al. suggested that one reason why Sr_2CaReO_6 has the strong antiferromagnetic interaction is due to the extended nature of the $5d$ orbitals, which provide good overlap [22]. The smaller J_1/k_B for Ba compounds may be due to the disturbance of such overlap by the substitution of larger Ba for Sr.

Table 2
Transition temperatures (T_N), effective magnetic moments (μ_{eff}), theoretical magnetic moments for spin only ($\mu_{S.O.}$) and Weiss constants (θ) of Ba_2CaMO_6 (M = Re, Os)

	T_N (K)	μ_{eff} (μ_B)	$\mu_{S.O.}$ (μ_B)	θ (K)
Ba_2CaReO_6	15.4	0.744 (2)	1.73	−38.8 (6)
Ba_2CaOsO_6	51	1.61 (1)	2.83	−157 (2)

Table 3
Nearest neighbor exchange constants J_1 for Ba_2CaMO_6 (M = Re, Os) and some analogous compounds

	S	θ (K)	J_1/k_B (K)	Ref.
Ba_2CaReO_6	1/2	−38.8	−6.47	This work
Ba_2CaOsO_6	1	−157	−9.81	This work
Ba_2LiOsO_6	1/2	−40.48	−6.75	[11]
Ba_2NaOsO_6	1/2	−32.45	−5.41	[11]
Sr_2MgReO_6	1/2	−426	−71	[21]
Sr_2CaReO_6	1/2	−443	−73.8	[22]

3.3. Specific heat

Fig. 8 shows the temperature dependence of the specific heat for Ba_2CaMO_6. For Ba_2CaReO_6 and Ba_2CaOsO_6, a λ-type specific heat anomaly is observed at 15 and 50 K, respectively, magnetic transition temperatures, which support that these magnetic transitions are antiferromagnetic transitions.

By differentiating the specific heat against temperature, we can observe a change in the slope of C_p vs. T curve for Ba_2CaWO_6 and Ba_2CaReO_6 at 220 and 145 K, respectively (see the insets of Fig. 8). These results support that the structural phase transition observed for Ba_2CaWO_6 and Ba_2CaReO_6 are the second order transition. In fact, there exists the group–subgroup relationship between $Fm\bar{3}m$ and $I4/m$, and $I4/m$ and $I2/m$ [16,17].

The magnetic specific heat C_{mag} is obtained by subtracting the contribution of the lattice specific heat C_{lat} from the total specific heat obtained from experiments. To estimate this C_{lat}, the specific heat for nonmagnetic isomorphic compounds is often used. Unfortunately, the nonmagnetic Ba_2CaWO_6 is not isostructural with Ba_2CaOsO_6. For such cases, a polynomial function of the temperature is sometimes used to estimate the lattice specific heat. However, no reasonable estimation could be performed because of the high magnetic transition temperature for Ba_2CaOsO_6: the magnetic entropy change S_{mag} for Ba_2CaOsO_6 cannot be discussed.

In the case of Ba_2CaReO_6, the following method was used to estimate its lattice specific heat [22]. The Debye temperature θ_D as a function of temperature was determined for Ba_2CaReO_6 and Ba_2CaWO_6, based on

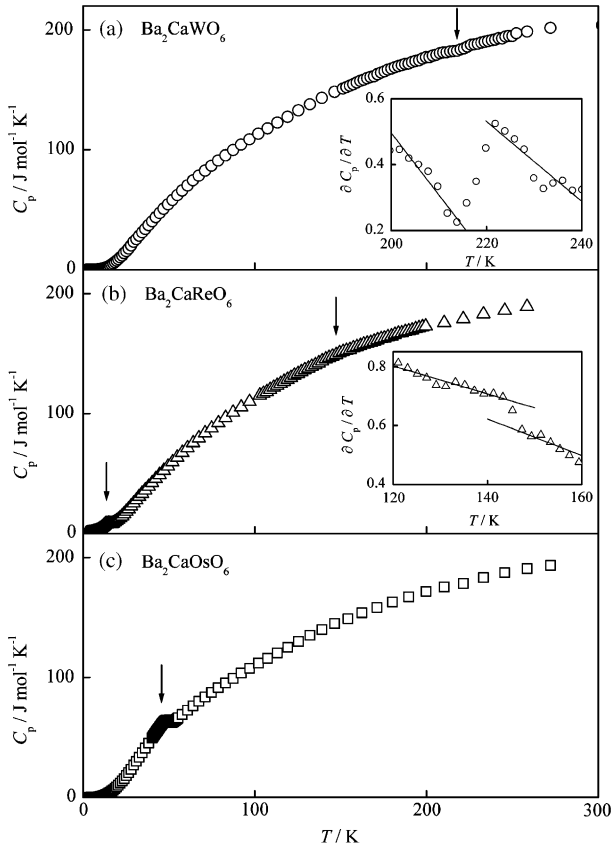

Fig. 8. Temperature dependences of the specific heat for Ba_2CaMO_6 (M = W, Re and Os). The insets of (a) and (b) show the differentials of the specific heat against temperature for Ba_2CaWO_6 between 200 and 240 K and for Ba_2CaReO_6 between 120 and 170 K, respectively. Solid lines are guides for the eye. Arrows show the temperatures at which specific heat anomalies are observed.

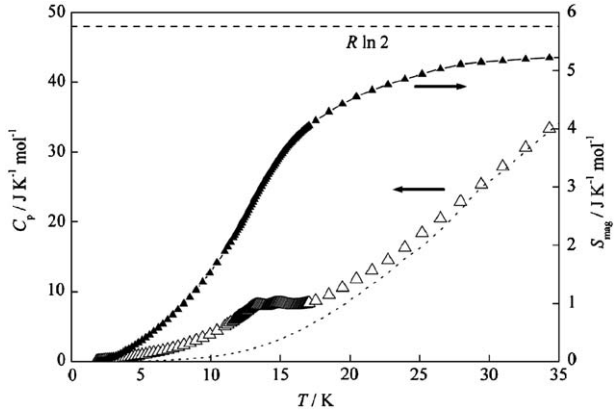

Fig. 9. Detailed specific heat (open triangle) and magnetic entropy (filled triangle) for Ba_2CaReO_6. A dotted line shows the lattice specific heat (see text). A dashed line shows the magnetic entropy change expected for $S = 1/2$.

the Debye model:

$$C_p = 9R(\theta_D/T)^3 \int_0^{\theta_D/T} \frac{x^4 e^x}{(e^x - 1)^2}\, dx. \quad (4)$$

The θ_D of Ba_2CaWO_6 was scaled by a single constant such that the value is consistent with that of Ba_2CaReO_6 at 50 K. The specific heat calculated from Eq. (4) with the scaled θ_D is used as the C_{lat} of Ba_2CaReO_6.

The magnetic entropy change S_{mag} associated with the magnetic transition is calculated by integrating:

$$S_{mag} = \int_0^T \frac{C_{mag}}{T}\, dT, \quad (5)$$

and $S_{mag} = 5.22\,J\,K^{-1}\,mol^{-1}$ is obtained (Fig. 9). This value is a little smaller than $R\ln 2$–$5.76\,J\,K^{-1}\,mol^{-1}$, where R is a molar gas constant. One reason for this is that the geometric frustration arising from the face-centered arrangement of the magnetic ions reduces the magnetic entropy change. It is reported that the magnetic properties for Sr_2MgReO_6 and Sr_2CaReO_6 characterized by the spin-glass behavior are due to the frustration, and that magnetic entropy changes are $0.167\,J\,K^{-1}\,mol^{-1}$ for Sr_2CaReO_6 and $3.73\,J\,K^{-1}\,mol^{-1}$ for Sr_2CaReO_6 [21,22]. These values are also smaller than the theoretical entropy change of $5.76\,J\,K^{-1}\,mol^{-1}$.

Acknowledgments

Fig. 5 was drawn with VENUS developed by Dilanian and Izumi. This work was supported by Grant-in-aid for Scientific Research of Priority Areas "Panoscopic Assembling and High Ordered Function for Rare Earth Materials" No. 17042003 from the Ministry of Education, Science, Sports, and Culture of Japan.

References

[1] M. Hanawa, Y. Muraoka, T. Tayama, T. Sakakibara, J. Yamamura, Z. Hiroi, Phys. Rev. Lett. 87 (2001) 187001.
[2] S. Yonezawa, Y. Muraoka, Y. Matsushita, Z. Hiroi, J. Phys.: Condens. Matter 16 (2004) L9.
[3] S. Yonezawa, Y. Muraoka, Y. Matsushita, Z. Hiroi, J. Phys. Soc. Jpn. 73 (2004) 819.
[4] S. Yonezawa, Y. Muraoka, Z. Hiroi, J. Phys. Soc. Jpn. 73 (2004) 1655.
[5] R. Ward, J. Longo, J. Am. Chem. Soc. 82 (1960) 5958.
[6] J. Longo, R. Ward, J. Am. Chem. Soc. 83 (1961) 2816.
[7] W. Prellier, V. Smolyaninova, A. Biswas, C. Galley, R.L. Greene, K. Ramesha, J. Gopalakrishnan, J. Phys.: Condens. Matter 12 (2000) 965.
[8] M. Abe, T. Nakagawa, S. Nomura, J. Phys. Soc. Jpn. 35 (1973) 1360.
[9] K.-I. Kobayashi, T. Kimura, Y. Tomioka, H. Sawada, K. Terakura, Y. Tokura, Phys. Rev. B 59 (1999) 11159.
[10] H. Kato, T. Okuda, Y. Okimoto, Y. Tomioka, K. Oikawa, T. Kamiyama, Y. Tokura, Phys. Rev. B 65 (2002) 144404.
[11] K.E. Stitzer, M.D. Smith, H.-C. Loye, Solid State Sci. 4 (2002) 311.
[12] E.G. Steward, H.P. Rooksby, Acta Crystallogr. 4 (1951) 503.
[13] W. Sleight, J. Longo, R. Ward, Inorg. Chem. 1 (1962) 245.
[14] F. Izumi, T. Ikeda, Mater. Sci. Forum 198 (2000) 321.
[15] M. Gateshki, J.M. Igartua, J. Phys.: Condens. Matter 16 (2004) 6639.

[16] C.J. Howard, B.J. Kennedy, P.M. Woodward, Acta Crystallogr. B 59 (2003) 463.
[17] T. Hahn, International Tables for Crystallography, vol. A, fourth ed., Kluwer Academic Publisher, Dordrecht, 1996.
[18] A.M. Glazer, Acta Crystallogr. B 28 (1972) 3384.
[19] P.M. Woodward, Acta Crystallogr. B 53 (1997) 32.
[20] R.D. Shannon, Acta Crystallogr. A 32 (1976) 751.
[21] C.R. Wiebe, J.E. Greedan, P.P. Kyriakou, G.M. Luke, J.S. Gardner, A. Fukaya, I.M. Gat-Malureanu, P.L. Russo, A.T. Savici, Y.J. Uemura, Phys. Rev. B 68 (2003) 134410.
[22] C.R. Wiebe, J.E. Greedan, G.M. Luke, J.S. Gardner, Phys. Rev. B 65 (2002) 144413.
[23] J.S. Smart, Effective Field Theories of Magnetism, Saunders, Philadelphia, 1966.